Description of the multinucleon transfer mechanism for ^{48}Ca + ^{244}Pu and ^{86}Kr + ^{198}Pt reactions in a quantal transport approach

M. Arik [1], S. Ayik [2,*], O. Yilmaz [1], and A. S. Umar [3]

[1] *Physics Department, Middle East Technical University, 06800 Ankara, Turkey*

[2] *Physics Department, Tennessee Technological University, Cookeville, Tennessee 38505, USA*

[3] *Department of Physics and Astronomy, Vanderbilt University, Nashville, Tennessee 37235, USA*

(Received 30 August 2023; accepted 9 November 2023; published 12 December 2023)

Background: Multinucleon transfer (MNT) reactions involving heavy projectile and target combinations stand as a promising method for synthesizing new neutron-rich exotic nuclei, which may not be possible using hot or cold fusion reactions or fragmentation. Exploring the mechanisms behind MNT reactions is essential and it requires a comprehensive theoretical framework that can explain the physical observables in these reactions.

Purpose: This work aims to show that the quantal diffusion approach based on the stochastic mean-field (SMF) theory is capable of explaining the reaction dynamics observed in MNT reactions. Primary product mass distributions in ^{48}Ca + ^{244}Pu reaction at $E_{\text{c.m.}} = 203.2$ MeV and ^{86}Kr + ^{198}Pt reaction at $E_{\text{c.m.}} = 324.2$ MeV are calculated and compared with the available experimental data.

Methods: In this work, we utilize the time-dependent Hartree-Fock (TDHF) calculations to analyze the mean-field reaction dynamics computationally in the reactions ^{48}Ca + ^{244}Pu and ^{86}Kr + ^{198}Pt for a broad range of initial angular momenta. Quantal transport description based on the SMF approach is used to calculate quantal diffusion coefficients and mass variances in ^{48}Ca + ^{244}Pu and ^{86}Kr + ^{198}Pt systems. The primary products arising from quasifission reactions are described by joint probability distribution in the SMF approach and those arising from fusion-fission are estimated by using the statistical deexcitation code GEMINI++.

Results: Mean values of charge and mass numbers, scattering angles of the primary reaction products, and the total kinetic energies after the collision are calculated within the TDHF framework for a broad range of initial angular momenta. Throughout all the collisions, drift toward the mass symmetry and large mass dispersion associated with this drift are observed. The calculated primary fragment and mass distributions using the SMF approach successfully explain experimental observations for the ^{48}Ca + ^{244}Pu and ^{86}Kr + ^{198}Pt systems.

Conclusions: The primary mass distributions, mean values of binary products, and mass dispersions are determined and results are compared with the available experimental data. The observed agreement between the experimental data and SMF results highlights the effectiveness of the quantal diffusion mechanism based on the SMF approach, which does not include any adjustable parameters other than standard parameters of Skyrme energy density functional.

DOI: 10.1103/PhysRevC.108.064604

I. INTRODUCTION

Over the last decade, the number of isotopes in the chart of nuclides has increased significantly. Although there has been a great effort to synthesize superheavy elements and exotic isotopes such as neutron-rich or proton-rich isotopes, the relatively low cross sections of these isotopes still impose a difficult challenge in heavy-ion experiments. Superheavy elements produced so far have been a product of either hot [1,2] or cold fusion [3] reactions, wherein the highly excited compound nuclei deexcite mostly by neutron emission and secondary fission. As an alternative, multinucleon transfer (MNT) in heavy-ion collisions is a promising approach for the synthesis of new neutron-rich nuclei. For this purpose, MNT reactions involving heavy projectile and target combinations have been extensively studied experimentally near barrier energies over the last few years [4–17]. In quasifission reactions involving heavy nuclei, ions stick together to form a dinuclear system. During this period, a large number of nucleons are transferred between the colliding ions. It has been experimentally observed that entrance channel properties such as N/Z ratio, the presence of entrance-channel magicity (the number of spherical shells in the reaction entrance channel) [18], relative orientation of deformed ions [19–23], and the charge product $Z_P Z_T$ [24–28] could have a significant effect on the reaction outcome. Although quasifission reactions usually favor transfer towards mass symmetry, it has been experimentally observed that nucleon transfer from lighter to heavier ions is also possible [5,7,29].

Exploring the mechanisms behind multinucleon transfer reactions requires a comprehensive theoretical framework that can properly account for these intricate processes. The time-dependent Hartree-Fock (TDHF) theory provides a

*ayik@tntech.edu

microscopic description of reaction dynamics and it has been employed extensively to analyze MNT reactions [30–38] (see Refs. [39–42] for recent reviews of TDHF applications to heavy-ion reactions). In TDHF theory, it is possible to calculate the physical dynamical observables, such as the mean values of the fragment charge and mass, and the mean kinetic energy depletion arising from one-body dissipation [43]. Although the TDHF theory has shown that it is a strong candidate for exploring MNT reactions, it is unable to account for fluctuations and dispersions of the fragment mass and charge distributions. To overcome this limitation, one has to go beyond the mean-field approximation [44–48]. One such approach is through the time-dependent random phase approximation (TDRPA) developed by Balian and Vénéroni, which offers a reasonable theory to compute larger observable fluctuations beyond mean field. This method has been used to study multinucleon transfer reactions in symmetric systems [49–53], and was validated by comparing to experimental data. However, the method is limited to describe the dispersion of charge and mass distributions only for symmetric systems.

In analogy with TDRPA, the stochastic mean-field (SMF) theory, which was first proposed by Ayik in 2008 [47], provides an alternative extension to the mean-field approximation. The SMF theory goes beyond the TDHF method by including mean-field fluctuations and correlations into the description. This work aims to show that the quantal diffusion approach based on SMF theory can explain the reaction dynamics observed in $^{48}\mathrm{Ca}+{}^{244}\mathrm{Pu}$ reaction at $E_{\mathrm{c.m.}}=203.2$ MeV and $^{86}\mathrm{Kr}+{}^{198}\mathrm{Pt}$ reaction at $E_{\mathrm{c.m.}}=324.2$ MeV without any adjustable parameters other than standard Skyrme energy density functional parameters. The remainder of this paper is organized as follows. In Sec. II, we present TDHF calculations for $^{48}\mathrm{Ca}+{}^{244}\mathrm{Pu}$ reaction at $E_{\mathrm{c.m.}}=203.2$ MeV and $^{86}\mathrm{Kr}+{}^{198}\mathrm{Pt}$ reaction at $E_{\mathrm{c.m.}}=324.2$ MeV. In Sec. III, we briefly discuss the quantal transport theory based on the SMF approach and discuss the SMF results for both systems. In Sec. IV, we present the primary product mass distributions for both reactions using the quantal diffusion approach based on the SMF theory and compare our results with the available experimental data [27,54]. In Sec. V, conclusions are presented.

II. MEAN REACTION DYNAMICS IN TDHF

In Table I, we share the TDHF results for $^{48}\mathrm{Ca}+{}^{244}\mathrm{Pu}$ system at $E_{\mathrm{c.m.}}=203.2$ MeV for the tip orientation of the ^{244}Pu nucleus and $^{86}\mathrm{Kr}+{}^{198}\mathrm{Pt}$ system at $E_{\mathrm{c.m.}}=324.2$ MeV for the tip orientation of the ^{198}Pt nucleus for a range initial orbital angular momenta, ℓ_i, final values of mass and charge numbers of projectilelike A_1^f, Z_1^f and targetlike A_2^f, Z_2^f fragments, final total kinetic energy TKE, scattering angles in the center-of-mass frame $\theta_{\mathrm{c.m.}}$, and laboratory frame θ_1^{lab} and θ_2^{lab}, respectively. The calculations presented in the paper employed the TDHF code [56,57] using the SLy4d Skyrme energy density functional [58], with a box size of $60\times60\times36$ fm in the x-y-z directions. To reduce the computation time, we present quantities that are evaluated for every two units of initial angular momentum for $^{48}\mathrm{Ca}+{}^{244}\mathrm{Pu}$ system, and 20 units of initial angular momentum for $^{86}\mathrm{Kr}+{}^{198}\mathrm{Pt}$ system.

TABLE I. Results of the TDHF calculations for the $^{48}\mathrm{Ca}+{}^{244}\mathrm{Pu}$ system at $E_{\mathrm{c.m.}}=203.2$ MeV for the tip orientation of the ^{244}Pu nucleus and the $^{86}\mathrm{Kr}+{}^{198}\mathrm{Pt}$ system at $E_{\mathrm{c.m.}}=324.2$ MeV for the tip orientation of the ^{198}Pt nucleus.

ℓ_i ($\hbar$)	A_1^f	Z_1^f	A_2^f	Z_2^f	TKE	$\theta_{\mathrm{c.m.}}$	θ_1^{lab}	θ_2^{lab}
$^{48}\mathrm{Ca}+{}^{244}\mathrm{Pu}$ system at $E_{\mathrm{c.m.}}=203.2$ MeV								
44	88.9	35.4	203.1	78.6	218.8	94.9	78.8	53.7
46	88.4	35.1	203.6	78.9	217.8	89.1	73.4	57.6
48	89.4	35.0	203.6	79.0	216.6	84.0	68.6	61.4
50	88.2	35.0	203.8	79.0	217.2	79.7	64.9	64.3
52	87.7	34.9	204.3	79.1	218.3	76.7	62.4	66.5
54	87.6	34.9	204.4	79.1	218.4	74.1	60.1	68.5
56	87.9	35.1	204.1	78.9	216.9	70.9	57.2	71.0
58	86.8	34.7	205.2	79.3	215.2	66.9	53.8	73.6
60	83.8	35.5	208.2	80.5	214.8	62.2	50.1	76.4
62	88.7	35.5	203.3	78.5	215.6	56.3	44.7	83.4
64	92.1	36.6	199.9	77.4	211.1	43.6	34.1	-83.1
66	84.5	33.9	207.5	80.1	197.5	43.7	34.4	-88.5
68	80.8	32.5	211.2	81.5	190.0	57.4	45.7	76.4
70	65.0	26.5	227.0	87.5	168.2	75.1	61.9	55.9
$^{86}\mathrm{Kr}+{}^{198}\mathrm{Pt}$ system at $E_{\mathrm{c.m.}}=324.2$ MeV								
60	95.9	39.1	188.1	74.9	214.2	109.4	75.3	32.8
80	89.7	36.7	194.3	77.3	220.6	102.9	71.8	34.9
100	88.4	36.2	195.6	77.8	223.6	98.4	68.6	36.7
120	88.3	36.2	195.7	77.8	242.5	93.9	66.0	39.7

TDHF ground-state calculations show that ^{48}Ca and ^{86}Kr nuclei exhibit spherical shapes, whereas ^{244}Pu and ^{198}Pt nuclei exhibit strong prolate and oblate deformations, respectively. For this reason, to consider all possible relative orientations of the deformed nuclei, TDHF and SMF calculations were performed for all possible relative orientations of the reaction partners. As a convention, we denote the initial orientation of the target principal deformation axis to be along the collision axis direction as the tip, and the case when their principal axis is perpendicular to the collision axis as the side.

In Ref. [55], $^{48}\mathrm{Ca}+{}^{244}\mathrm{Pu}$ system is analyzed at two different energies, $E_{\mathrm{c.m.}}=193.3$ MeV and $E_{\mathrm{c.m.}}=203.2$ MeV, corresponding to $E_{\mathrm{c.m.}}/V_{\mathrm{Bass}}=0.98$ and $E_{\mathrm{c.m.}}/V_{\mathrm{Bass}}=1.03$, Similarly in Refs. [27,54], $^{86}\mathrm{Kr}+{}^{198}\mathrm{Pt}$ system is analyzed at $E_{\mathrm{c.m.}}=324.2$ MeV corresponding to $E_{\mathrm{c.m.}}/V_{\mathrm{Bass}}=1.12$. In these experiments, the reaction fragments for $^{48}\mathrm{Ca}+{}^{244}\mathrm{Pu}$ and $^{86}\mathrm{Kr}+{}^{198}\mathrm{Pt}$ systems were detected between 42°–78° and 30°–68° in the laboratory frame. The mass-energy distributions of the detected fragments are shown in Fig. 2 of Ref. [27] and Fig. 1 of Ref. [54]. In these figures, red continuous contours were used to exclude elastic events and select events arising from either MNT or fissionlike reactions. In order to determine the initial angular momenta intervals corresponding to the experimental windows, the TKE vs. mass value is scattered in the TKE-mass plane for each calculated initial angular momentum value and the resultant distribution is plotted for both systems in Fig. 1. Red continuous contours represent the gates used in the experiments in Refs. [27,54,55]. By considering the mean-field calculations shown in Fig. 1 and the scattering angles in the laboratory frame, θ_1^{lab} and θ_2^{lab}, given

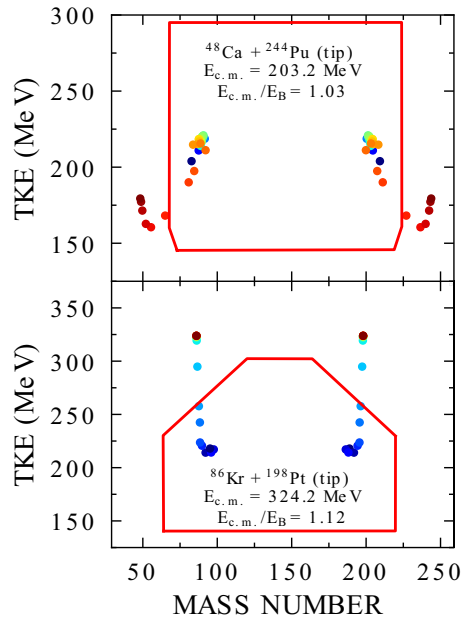

FIG. 1. Mass-energy distributions of fragments obtained by TDHF calculations for the $^{48}\mathrm{Ca}+^{244}\mathrm{Pu}$ system at $E_{\mathrm{c.m.}} = 203.2$ MeV and the $^{86}\mathrm{Kr}+^{198}\mathrm{Pt}$ system at $E_{\mathrm{c.m.}} = 324.2$ MeV. Red continuous contours represent the gates used in the experiments in Refs. [27,54,55].

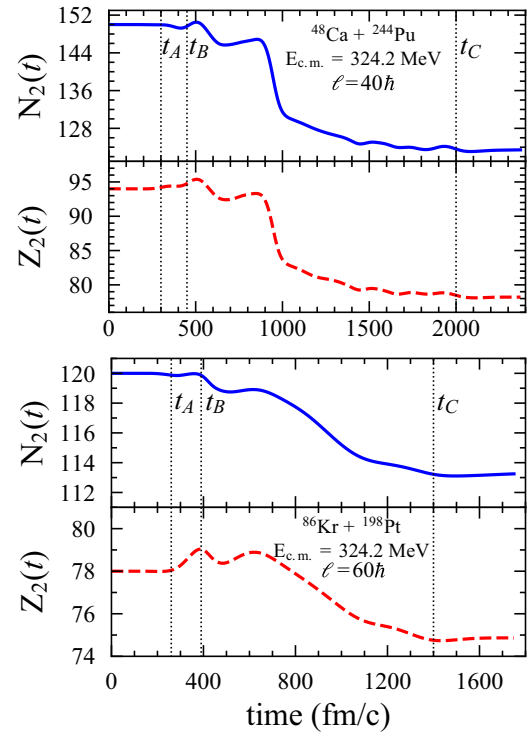

FIG. 2. Mean values of neutron and proton numbers of targetlike fragments at initial angular momentum $\ell_i = 40\hbar$ for $^{48}\mathrm{Ca}+^{244}\mathrm{Pu}$ system at $E_{\mathrm{c.m.}} = 203.2$ MeV and $\ell_i = 60\hbar$ for $^{86}\mathrm{Kr}+^{198}\mathrm{Pt}$ system at $E_{\mathrm{c.m.}} = 324.2$ MeV are shown as a function of time. Solid blue lines denote the neutron numbers and dashed red lines denote the proton numbers of targetlike fragments. The labels t_A, t_B, and t_C indicate the projection of the time intervals used to determine the curvature parameters.

in Table I, we determined that the initial angular momenta range to be $44\hbar \leqslant \ell_i \leqslant 70\hbar$ for the $^{48}\mathrm{Ca}+^{244}\mathrm{Pu}$ system and $60\hbar \leqslant \ell_i \leqslant 120\hbar$ for the $^{86}\mathrm{Kr}+^{198}\mathrm{Pt}$ system, corresponding to the angular coverage range in these experiments [27,54,55]. For the side orientation of the target nuclei, we observed that the primary binary products do not satisfy the angular range and TKE-mass region conditions related to the experimental setup mentioned above at the same time. Thus, in this study, calculations for side orientations were excluded.

If we denote the charge asymmetry of the reaction fragments with $\delta = \frac{N-Z}{A}$, the charge asymmetry values of the reaction partners are found to be $\delta(\mathrm{Ca}) \simeq 0.17$, $\delta(\mathrm{Pu}) \simeq 0.23$, $\delta(\mathrm{Kr}) \simeq 0.16$, and $\delta(\mathrm{Pt}) \simeq 0.21$. When reaction partners have different charge asymmetries, particularly during the initial phase of the collision, reaction partners quickly exchange few nucleons to reach the same charge asymmetry value. Subsequently, the reaction partners continue to exchange nucleons and the system drifts along the nearly constant charge asymmetry line in the (N-Z) plane, which we call the isoscalar line. As an example of the reaction dynamics calculated within TDHF framework, we present the time evolution of the neutron $N(t)$ and proton $Z(t)$ numbers of targetlike fragments in $^{48}\mathrm{Ca}+^{244}\mathrm{Pu}$ at $\ell_i = 40\hbar$ and $^{86}\mathrm{Kr}+^{198}\mathrm{Pt}$ system at $\ell_i = 60\hbar$ in Fig. 2. To gain more insight into these systems, we can easily eliminate the time dependence of neutron $N(t)$ and proton $Z(t)$ numbers and plot the collision dynamics in the (N-Z) plane. In the resultant Fig. 3, thick blue lines show the mean drift path of the targetlike fragments, whereas the dashed lines show the isoscalar lines corresponding to each system. The angle ϕ between the N plane and isoscalar path was found to be $\phi = 32.0^\circ$ and $\phi = 32.5^\circ$ for each system. In both systems, the isoscalar line extends from the lighter reaction partner up to a heavier reaction partner, passing through the mass symmetry point (N_0, Z_0), where $N_0 = (N_1 + N_2)/2$. As we can clearly see in Fig. 3, because the charge asymmetries of the initial reaction partners differ in both systems, both systems initially quickly drift towards the isoscalar line. The reaction partners then drift along the stability line toward the mass symmetry point. In Figs. 2 and 3, labels t_A, t_B, and t_C indicate the time labels used in calculating the reduced curvature parameters, which will be explained in Sec. III C. Lastly, within the given initial angular momentum intervals, the mean reaction times are roughly equal to 6 zs for the $^{48}\mathrm{Ca}+^{244}\mathrm{Pu}$ system, and 3 zs for the $^{86}\mathrm{Kr}+^{198}\mathrm{Pt}$ system, which is consistent with the predictions in Refs. [27,59].

III. QUANTAL DIFFUSION DESCRIPTION

A. Langevin equation for macrovariables

In the TDHF approach, with a given set of initial conditions, a single-particle density matrix is calculated by a single Slater determinant. In the SMF approach, the collision dynamics are described in terms of an ensemble of the mean-field events [47,48,60]. In each event, the complete set of single-particle wave functions is determined by the TDHF

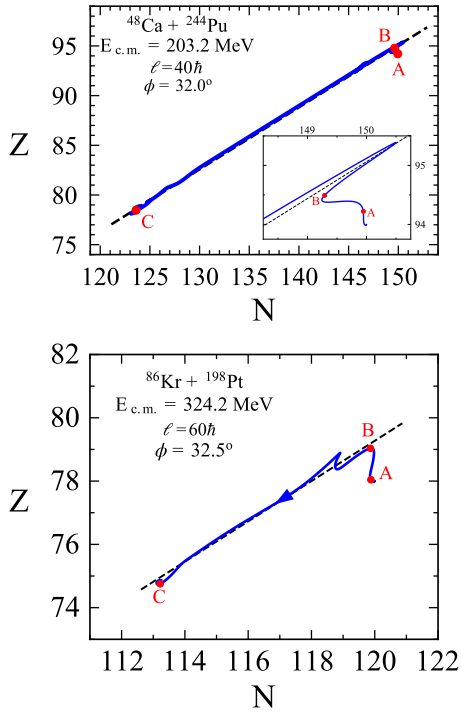

FIG. 3. Mean drift path in the N-Z plane for the targetlike fragments are given at initial angular momentum $\ell_i = 40\hbar$ for ^{48}Ca + ^{244}Pu system at $E_{\text{c.m.}} = 203.2$ MeV and $\ell_i = 60\hbar$ for ^{86}Kr + ^{198}Pt system at $E_{\text{c.m.}} = 324.2$ MeV. Solid blue lines denote the mean drift path and dashed black lines denote the isoscalar lines. The labels A, B, and C indicate the projection of the time intervals used to determine the curvature parameters.

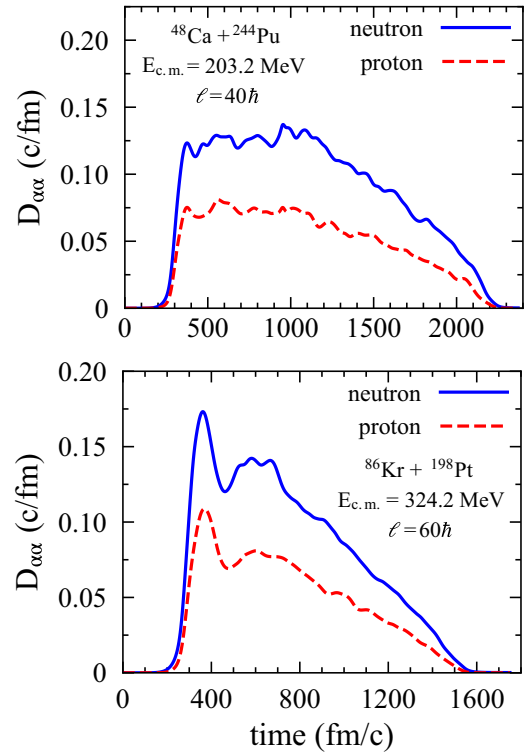

FIG. 4. Diffusion coefficient for neutron and proton transfers at initial angular momentum $\ell = 40\hbar$ for ^{48}Ca + ^{244}Pu system at $E_{\text{c.m.}} = 203.2$ MeV, and $\ell = 60\hbar$ for ^{86}Kr + ^{198}Pt system at $E_{\text{c.m.}} = 324.2$ MeV are shown as a function of time. Solid blue lines denote the diffusion coefficients of neutron transfer, $D_{NN}(t)$; dashed red lines denote the diffusion coefficients of proton transfer, $D_{ZZ}(t)$.

equations with the self-consistent Hamiltonian of that event. The ensemble is considered to be generated by incorporating the quantal and thermal fluctuations at the initial state. We consider low-energy collisions at which a dinuclear structure is maintained during the collision. The identities of colliding nuclei are preserved to a large extent, but nucleon transfer takes place between targetlike and projectilelike nuclei. With the help of geometric projection, for small amplitude fluctuations, we derive the linearized coupled Langevin equations (Eq. (7) in Ref. [60]) for macroscopic variables. For further explanation of Langevin equation for macroscopic variables in nuclear reactions, we refer the reader to Sec. 1A in the online Supplemental Material [60].

B. Quantal diffusion coefficients

According to the SMF approach, stochastic parts of drift coefficients (given by Eq. (8) in Ref. [60]) have Gaussian random distributions with zero mean values, $\delta\bar{v}_p^{\lambda}(t) = 0$, $\delta\bar{v}_n^{\lambda}(t) = 0$ with the autocorrelation functions, which are integrated over the history, determining the diffusion coefficients $D_{\alpha\alpha}(t)$ for proton and neutron transfers. Usually, to calculate the quantal diffusion coefficients, one needs to sum over the whole particle and hole states. But in the diabatic limit, we can get rid of the particle states by utilizing closure relations and calculate the diffusion coefficients only in terms of the occupied single-particle states of the TDHF calculations. This is consistent with the dissipation-fluctuation theorem of nonequilibrium statistical mechanics. The explicit expression for the quantal diffusion coefficients is given in Eq. (10) in the online Supplemental Material [60]. Such a quantal expression for the nucleon diffusion coefficient in heavy-ion collisions is given in the literature for the first time from a microscopic basis.

In Fig. 4, the diffusion coefficients for neutron and proton transfers are shown. The quantal diffusion coefficients were calculated using Eq. (10) in online Supplemental Material [60] (see also Refs. [61,62]), for each initial angular momentum. As shown in the figure, the neutron diffusion coefficients are almost twice the value of the proton diffusion coefficients. This is mainly due to the Coulomb repulsion between the protons and the total neutron number of the colliding system being far greater than the total proton number. This behavior is also observed in different heavy-ion reactions in which the SMF theory is employed [63–70].

C. Reduced curvature parameters

After the colliding nuclei form a dinuclear system, the nucleon drift mechanism is mainly determined via the potential energy surface projected in the (N-Z) plane. TDHF theory includes different energy contributions microscopically such as surface energy, electrostatic energy, symmetry energy, and

TABLE II. Calculated reduced curvature parameters for ^{48}Ca + ^{244}Pu system at $E_{\rm c.m.} = 203.2$ MeV and ^{86}Kr + ^{198}Pt system at $E_{\rm c.m.} = 324.2$ MeV. The time intervals t_A and t_B are used to calculate the isovector reduced curvature parameter α using Eqs. (27), (28) of Ref. [60]. The time intervals t_B and t_C are used to calculate the isoscalar-reduced curvature parameter, β, using Eqs. (25), (26) of Ref. [60]. These time labels are also shown in Figs. 2 and 3.

System	t_A (fm/c)	t_B (fm/c)	t_C (fm/c)	α	β
^{48}Ca + ^{244}Pu	300	425	2000	0.156	0.004
^{86}Kr + ^{198}Pt	260	390	1400	0.176	0.003

centrifugal potential energy. In SMF theory, we approximate the shape of the potential energy in the (N-Z) plane near the local equilibrium state in terms of two parabolic forms, given by Eq. (18) in Ref. [60]. By using Einstein relations in the overdamped limit [63,67,69,71,72] and inverting Eq. (17) of Ref. [60], we can derive Eqs. (25)–(28) to calculate reduced curvature parameters.

As we briefly mentioned in Sec. II, to calculate the reduced curvature parameters related to each system, we considered the collision at $\ell_i = 40\hbar$ for ^{48}Ca + ^{244}Pu system and collision at $\ell_i = 60\hbar$ for ^{86}Kr + ^{198}Pt system. By using Eqs. (25)–(28) in Ref. [60], we can calculate the isoscalar and isovector reduced curvature parameters related to each system. In Table II, we tabulate the calculated values of reduced curvature parameters and time intervals related to each system. The local equilibrium state (N_0, Z_0) in Eqs. (26), (28) in Ref. [60] is taken as mass symmetry point $(N_0, Z_0) = (N_T/2, Z_T/2)$ for both systems; where its value is equal to $(N_0, Z_0) = (89, 57)$ for the ^{48}Ca + ^{244}Pu system and $(N_0, Z_0) = (85, 57)$ for the ^{86}Kr + ^{198}Pt system.

D. Covariances of fragment charge and mass distributions

Primary mass distribution is found by using the standard expression

$$Y(A)^{\rm MNT} = \frac{1}{\sum_{\ell_{\rm min}}^{\ell_{\rm max}}(2l+1)} \sum_{\ell_{\rm min}}^{\ell_{\rm max}} (2\ell+1) P_\ell(A). \quad (1)$$

Here, $P_\ell(A)$ is given by

$$P_\ell(A) = \tfrac{1}{2}\left[P_\ell^{\rm pro}(A) + P_\ell^{\rm tar}(A)\right], \quad (2)$$

where $P_\ell^{\rm pro}(A)$ and $P_\ell^{\rm tar}(A)$ denote the normalized probabilities of producing projectilelike and targetlike fragments, respectively. A factor of 1/2 was introduced to normalize the total primary fragment distribution to unity. In Eq. (2), probabilities are given by

$$P_\ell^{\rm pro,tar}(A) = \frac{1}{\sqrt{2\pi}} \frac{1}{\sigma_{AA}^2(\ell)} \exp\left[-\frac{1}{2}\left(\frac{A - A_\ell^{\rm pro,tar}}{\sigma_{AA}^2(\ell)}\right)^2\right]. \quad (3)$$

Here, the probability distribution of the mass number of produced fragments is determined by summing over N or Z and keeping the total mass number constant $A = N + Z$ in correlated Gaussian function Eq. (29) in Ref. [60]. In

TABLE III. Results of the SMF calculations for the ^{48}Ca + ^{244}Pu system at $E_{\rm c.m.} = 203.2$ MeV in tip configuration of ^{244}Pu nucleus and the ^{86}Kr + ^{198}Pt system at $E_{\rm c.m.} = 324.2$ MeV in tip configuration of ^{198}Pt nucleus.

ℓ_i ($\hbar$)	σ_{NN}	σ_{ZZ}	σ_{NZ}	σ_{AA}
	^{48}Ca + ^{244}Pu system at $E_{\rm c.m.} = 203.2$ MeV			
44	11.6	7.4	8.9	18.7
46	11.6	7.5	8.9	18.7
48	11.7	7.5	9.0	18.8
50	11.7	7.5	9.0	18.8
52	11.7	7.5	8.9	18.8
54	11.6	7.4	8.9	18.6
56	11.5	7.4	8.8	18.5
58	11.4	7.3	8.8	18.4
60	11.5	7.4	8.8	18.5
62	11.5	7.4	8.8	18.5
64	11.9	7.6	9.2	19.2
66	11.5	7.4	8.8	18.5
68	10.6	6.8	8.1	17.0
70	8.9	5.8	6.7	14.2
	^{86}Kr + ^{198}Pt system at $E_{\rm c.m.} = 324.2$ MeV			
60	10.3	6.7	8.0	16.7
80	8.5	5.6	6.4	13.7
100	7.2	4.8	5.3	11.5
120	5.9	4.0	4.1	9.2

Eq. (3), the mass variance is given by $\sigma_{AA}^2(\ell) = \sigma_{NN}^2(\ell) + \sigma_{ZZ}^2(\ell) + 2\sigma_{NZ}^2(\ell)$, where $\sigma_{NN}^2(\ell)$, $\sigma_{ZZ}^2(\ell)$, and $\sigma_{NZ}^2(\ell)$ stand for neutron, proton, and mixed dispersions, respectively. By using the calculated reduced curvature parameters and quantal diffusion coefficients for proton and neutron transfer, we can solve the coupled differential equations (Eqs. (14)–(16) of Ref. [60] and Refs. [73,74]) to determine σ_{NN}^2, σ_{ZZ}^2, σ_{NZ}^2, and σ_{AA}^2 for each initial angular momentum with the initial conditions $\sigma_{NN} = \sigma_{ZZ} = \sigma_{NZ} = 0$ at $t = 0$. In Table III, we show the asymptotic values for neutrons σ_{NN}, protons σ_{ZZ}, mixed dispersions σ_{NZ}, and mass dispersions σ_{AA} calculated for each initial angular momentum value. As an example, the calculated neutron, proton, and mixed variances as a function of time in ^{48}Ca + ^{244}Pu reaction at $\ell_i = 40\hbar$ and ^{86}Kr + ^{198}Pt reaction at $\ell_i = 60\hbar$ are shown in Fig 5. In both systems, we see that during the initial phase of the reaction, up to about $t \simeq 500$ (fm/c), the magnitude of variances are in order as $\sigma_{NZ} < \sigma_{ZZ} < \sigma_{NN}$. After that the correlations evolve over time, changing the order to $\sigma_{ZZ} < \sigma_{NZ} < \sigma_{NN}$, demonstrating the importance of correlations arising from significant energy dissipation.

In the experiments of Refs. [27,54,55], it was observed that both quasifission and fusion-fission contribute to the mass-symmetric region near $(\frac{A_1+A_2}{2} \pm 20) \simeq (146 \pm 20)$ for both systems. By using the quantal diffusion approach [Eq. (1)], we can determine the fragment mass distribution due to the MNT mechanism (please see Eq. (29) in the online Supplemental Material [60] and Ref. [75]). Furthermore, to obtain information about the contribution from fusion-fission-like events, we can utilize the statistical Monte Carlo code GEMINI++ [76]

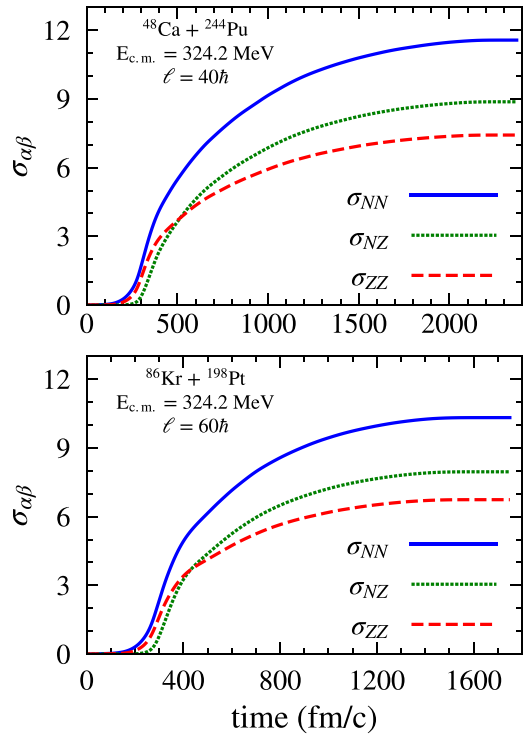

FIG. 5. Neutron, proton, and mixed variances as a function of time at initial angular momentum $\ell = 40\hbar$ for ^{48}Ca + ^{244}Pu system at $E_{\text{c.m.}} = 203.2$ MeV, and $\ell = 60\hbar$ for ^{86}Kr + ^{198}Pt system at $E_{\text{c.m.}} = 324.2$ MeV. Solid blue lines denote the neutron variances, σ_{NN}; dashed red lines denote the proton variances, σ_{ZZ}; and dotted green lines denote the mixed variances, σ_{NZ}.

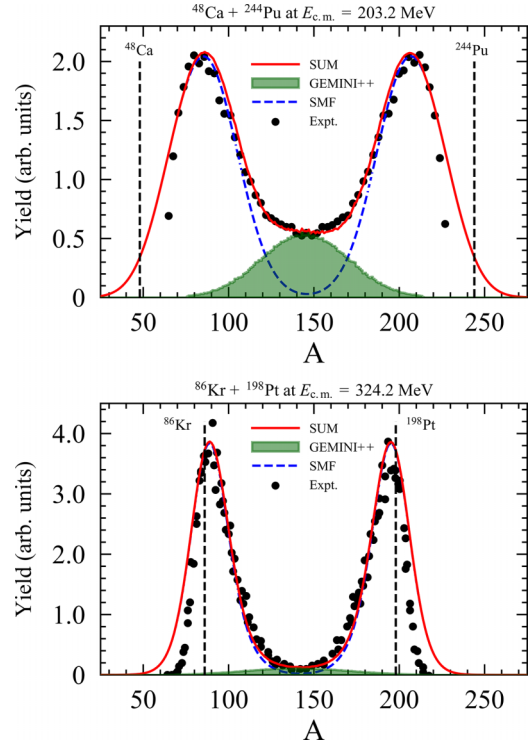

FIG. 6. Primary fragment yield in the ^{48}Ca + ^{244}Pu system at $E_{\text{c.m.}} = 203.2$ MeV and ^{86}Kr + ^{198}Pt system at $E_{\text{c.m.}} = 324.2$ MeV in tip orientation of targetlike nuclei. The experimental data obtained from Refs. [27,54] are indicated by the closed black circles. Dashed blue lines indicate the primary product mass distributions calculated within the SMF framework. The fusion-fission fragment distribution indicated by the green filled area was calculated using the GEMINI++ code [76]. The summation of yield distribution calculated by the SMF approach and GEMINI++ are indicated by solid red lines.

for this region. The excitation energy of the compound nuclei ^{284,292}Fl is estimated by, $E^*_{\text{CN}} = E_{\text{c.m.}} + Q_{gg}$, where Q_{gg} stands for released disintegration energy in fusion reaction. Combined with GEMINI++, total primary fragment mass distribution takes the form

$$Y(A)^{\text{sum}} = [\eta^{\text{MNT}} Y(A)^{\text{MNT}} + \eta^{FF} Y(A)^{FF}], \tag{4}$$

where $Y(A)^{FF}$ stands for the probability of reaching fission fragment with mass number A, after the statistical deexcitation of superheavy flerovium compound nucleus. The reliability of this method is discussed and verified in the next section, Sec. IV. In GEMINI++ calculations, the number of simulation times is set to $M_{\text{trial}} = 100\,000$, which is sufficient to get a statistical distribution for this region. In Eq. (4), η^{MNT} and η^{FF} stand for normalizing constants for distributions arising from the MNT reaction and fission reaction, respectively. The value of η^{MNT} is determined by matching the peak values of experimental yield [27] at $A \approx 208$ to give value $\eta^{\text{MNT}} = 202$ for ^{48}Ca + ^{244}Pu system and peak value of experimental yield [54] at $A \approx 200$ to give value $\eta^{\text{MNT}} = 225$ for ^{86}Kr + ^{198}Pt system. Similarly, for fusion-fission reactions, the value of η^{FF} is determined by matching the experimental yield at $A \approx 146$ for both systems to give value $\eta^{\text{FF}} = 17$ for ^{48}Ca + ^{244}Pu system and $\eta^{\text{FF}} = 4$ for ^{86}Kr + ^{198}Pt system.

IV. PRIMARY PRODUCT MASS DISTRIBUTIONS

In Fig. 6, we share the calculated primary product distributions for ^{48}Ca + ^{244}Pu system at $E_{\text{c.m.}} = 203.2$ MeV and ^{86}Kr + ^{198}Pt system at $E_{\text{c.m.}} = 324.2$ MeV in tip orientation of targetlike nuclei and compare the results with the experimental data available [27,54]. Dashed blue lines indicate primary product mass distribution calculated within the SMF framework, whereas filled green areas represent the fusion-fission fragment distribution calculated using the GEMINI++ code [76]. The summation of yield distribution calculated by Eq. (4) is indicated by solid red lines. For comparison, the positions of initial reaction partners are shown by vertical dashed black lines in Fig. 6.

First, we can start by comparing the results obtained from the SMF approach for both systems. In Fig. 6, we can see that the SMF approach is well capable of explaining the mass distribution arising from the MNT reactions near the peak values. In the vicinity of the peak position, around 40 nucleons are transferred for ^{48}Ca + ^{244}Pu system, and around five nucleons are transferred for the ^{86}Kr + ^{198}Pt system. The SMF approach can clearly predict the peak position of the mass distribution for both systems. Furthermore, in ^{48}Ca + ^{244}Pu system, the SMF approach is able to explain the transfer

channels up to ≈55 nucleon transfer, up until $A \approx 100$ for projectilelike fragments ($A \approx 190$ for targetlike fragments). Similarly, in $^{86}\mathrm{Kr} + ^{198}\mathrm{Pt}$ system, since the contributions from fusion-fission are much lower, and MNT reactions are dominant, the SMF approach agrees quite well with the experimental data. We have to mention that, since the primary mass probability $P_\ell(A)$ in Eq. (2) is normalized to unity, the value normalization constant η also determines the integrated yield value under the mass-distribution functions in Fig. 6. In order to compare the contributions from fusion-fission in these systems we can calculate the ratio of integrated yield between the interval $A_{\mathrm{CN}} \pm 20$ to the total integrated yield under the experimental values. In $^{48}\mathrm{Ca} + ^{244}\mathrm{Pu}$ system, the interval for experimental data is taken as $65 \leqslant A \leqslant 225$, and the interval $A_{\mathrm{CN}} \pm 20$ region is taken as $126 \leqslant A \leqslant 166$ to give the value $22.3/201.3 \approx \%11$. Similarly, in $^{86}\mathrm{Kr} + ^{198}\mathrm{Pt}$ system, the interval for experimental data is taken as $65 \leqslant A \leqslant 215$, and the interval $A_{\mathrm{CN}} \pm 20$ region is taken as $122 \leqslant A \leqslant 162$ to give the value $6.5/225.4 \approx \%3$. Both results are consistent with the experimental results reported in Refs. [27,54]. This result clearly supports the idea that at energies above the Bass barrier, the MNT reactions dominate fusion-fission reactions with increasing Coulomb factor, $Z_P Z_T$.

V. CONCLUSIONS

In this work, we consider the charge and mass number as the macroscopic variables and utilize the quantal diffusion approach based on the SMF theory to calculate primary fragment mass distributions in $^{48}\mathrm{Ca} + ^{244}\mathrm{Pu}$ reaction at $E_{\mathrm{c.m.}} = 203.2$ MeV and $^{86}\mathrm{Kr} + ^{198}\mathrm{Pt}$ reaction at $E_{\mathrm{c.m.}} = 324.2$ MeV. The quantal diffusion coefficients associated with charge and mass variables are evaluated only in terms of the time-dependent single-particle wave functions of TDHF theory. The description includes the full collision geometry, quantal effects due to shell structure, and the Pauli exclusion principle. We emphasize that the SMF theory does not involve any adjustable parameters other than the standard parameters of energy density functional employed in TDHF theory. The calculated primary product mass distributions are compared with the experimental data for both systems. The observed agreement between the experimental data and SMF results highlight the effectiveness of the quantal diffusion approach based on the SMF approach.

ACKNOWLEDGMENTS

S.A. gratefully acknowledges Middle East Technical University for the warm hospitality extended to him during his visits. S.A. also gratefully acknowledges F. Ayik for continuous support and encouragement. This work is supported in part by US DOE Grants No. DE-SC0015513 and No. DE-SC0013847. This work is supported in part by TUBITAK Grant No. 122F150. The numerical calculations reported in this paper were partially performed at TUBITAK ULAKBIM, High Performance and Grid Computing Center (TRUBA resources).

[1] Yu. Ts. Oganessian, V. K. Utyonkov, Yu. V. Lobanov, F. Sh. Abdullin, A. N. Polyakov, R. N. Sagaidak, I. V. Shirokovsky, Yu. S. Tsyganov, A. A. Voinov, G. G. Gulbekian, S. L. Bogomolov, B. N. Gikal, A. N. Mezentsev, S. Iliev, V. G. Subbotin, A. M. Sukhov, K. Subotic, V. I. Zagrebaev, G. K. Vostokin, M. G. Itkis *et al.*, Synthesis of the isotopes of elements 118 and 116 in the $^{249}\mathrm{Cf}$ and $^{245}\mathrm{Cm} + ^{48}\mathrm{Ca}$ fusion reactions, Phys. Rev. C **74**, 044602 (2006).

[2] M. G. Itkis, G. N. Knyazheva, I. M. Itkis, and E. M. Kozulin, Experimental investigation of cross sections for the production of heavy and superheavy nuclei, Eur. Phys. J. A **58**, 178 (2022).

[3] S. Hofmann and G. Münzenberg, The discovery of the heaviest elements, Rev. Mod. Phys. **72**, 733 (2000).

[4] E. M. Kozulin, E. Vardaci, G. N. Knyazheva, A. A. Bogachev, S. N. Dmitriev, I. M. Itkis, M. G. Itkis, A. G. Knyazev, T. A. Loktev, K. V. Novikov, E. A. Razinkov, O. V. Rudakov, S. V. Smirnov, W. Trzaska, and V. I. Zagrebaev, Mass distributions of the system $^{136}\mathrm{Xe} + ^{208}\mathrm{Pb}$ at laboratory energies around the Coulomb barrier: A candidate reaction for the production of neutron–rich nuclei at $N = 126$, Phys. Rev. C **86**, 044611 (2012).

[5] E. M. Kozulin, G. N. Knyazheva, S. N. Dmitriev, I. M. Itkis, M. G. Itkis, T. A. Loktev, K. V. Novikov, A. N. Baranov, W. H. Trzaska, E. Vardaci, S. Heinz, O. Beliuskina, and S. V. Khlebnikov, Shell effects in damped collisions of $^{88}\mathrm{Sr}$ with $^{176}\mathrm{Yb}$ at the Coulomb barrier energy, Phys. Rev. C **89**, 014614 (2014).

[6] J. V. Kratz, M. Schädel, and H. W. Gäggeler, Reexamining the heavy-ion reactions $^{238}\mathrm{U} + ^{238}\mathrm{U}$ and $^{238}\mathrm{U} + ^{248}\mathrm{Cm}$ and actinide production close to the barrier, Phys. Rev. C **88**, 054615 (2013).

[7] Y. X. Watanabe, Y. H. Kim, S. C. Jeong, Y. Hirayama, N. Imai, H. Ishiyama, H. S. Jung, H. Miyatake, S. Choi, J. S. Song, E. Clement, G. de France, A. Navin, M. Rejmund, C. Schmitt, G. Pollarolo, L. Corradi, E. Fioretto, D. Montanari, M. Niikura *et al.*, Pathway for the production of neutron–rich isotopes around the $N = 126$ shell closure, Phys. Rev. Lett. **115**, 172503 (2015).

[8] H. M. Devaraja, S. Heinz, O. Beliuskina, V. Comas, S. Hofmann, C. Hornung, G. Münzenberg, K. Nishio, D. Ackermann, Y. K. Gambhir, M. Gupta, R. A. Henderson, F. P. Heßberger, J. Khuyagbaatar, B. Kindler, B. Lommel, K. J. Moody, J. Maurer, R. Mann, A. G. Popeko *et al.*, Observation of new neutron-deficient isotopes with $Z \geqslant 92$ in multinucleon transfer reactions, Phys. Lett. B **748**, 199 (2015).

[9] V. V. Desai, W. Loveland, K. McCaleb, R. Yanez, G. Lane, S. S. Hota, M. W. Reed, H. Watanabe, S. Zhu, K. Auranen, A. D. Ayangeakaa, M. P. Carpenter, J. P. Greene, F. G. Kondev, D. Seweryniak, R. V. F. Janssens, and P. A. Copp, The $^{136}\mathrm{Xe} + ^{198}\mathrm{Pt}$ reaction: A test of models of multi-nucleon transfer reactions, Phys. Rev. C **99**, 044604 (2019).

[10] B. Birkenbach, A. Vogt, K. Geibel, F. Recchia, P. Reiter, J. J. Valiente-Dobón, D. Bazzacco, M. Bowry, A. Bracco, B. Bruyneel, L. Corradi, F. C. L. Crespi, G. de Angelis, P. Désesquelles, J. Eberth, E. Farnea, E. Fioretto, A. Gadea, A. Gengelbach, A. Giaz *et al.*, Spectroscopy of the neutron-rich

actinide nucleus ^{240}U following multinucleon-transfer reactions, Phys. Rev. C **92**, 044319 (2015).

[11] A. Vogt, B. Birkenbach, P. Reiter, L. Corradi, T. Mijatović, D. Montanari, S. Szilner, D. Bazzacco, M. Bowry, A. Bracco, B. Bruyneel, F. C. L. Crespi, G. de Angelis, P. Désesquelles, J. Eberth, E. Farnea, E. Fioretto, A. Gadea, K. Geibel, A. Gengelbach *et al.*, Light and heavy transfer products in ^{136}Xe + ^{238}U multinucleon transfer reactions, Phys. Rev. C **92**, 024619 (2015).

[12] F. Galtarossa, L. Corradi, S. Szilner, E. Fioretto, G. Pollarolo, T. Mijatović, D. Montanari, D. Ackermann, D. Bourgin, S. Courtin, G. Fruet, A. Goasduff, J. Grebosz, F. Haas, D. Jelavić Malenica, S. C. Jeong, H. M. Jia, P. R. John, D. Mengoni, M. Milin *et al.*, Mass correlation between light and heavy reaction products in multinucleon transfer ^{197}Au + ^{130}Te collisions, Phys. Rev. C **97**, 054606 (2018).

[13] S. A. Kalandarov, G. G. Adamian, N. V. Antonenko, H. M. Devaraja, and S. Heinz, Production of neutron deficient isotopes in the multinucleon transfer reaction ^{48}Ca ($E_{\rm lab}$ = 5.63 MeV/nucleon) + ^{248}Cm, Phys. Rev. C **102**, 024612 (2020).

[14] C. Li, J. Tian, and F. Zhang, Production mechanism of the neutron-rich nuclei in multinucleon transfer reactions: A reaction time scale analysis in energy dissipation process, Phys. Lett. B **809**, 135697 (2020).

[15] G. G. Adamian, N. V. Antonenko, H. Lenske, L. A. Malov, and S. Zhou, Self-consistent methods for structure and production of heavy and superheavy nuclei, Eur. Phys. J. A **57**, 89 (2021).

[16] S. Heinz and H. M. Devaraja, Nucleosynthesis in multinucleon transfer reactions, Eur. Phys. J. A **58**, 114 (2022).

[17] Z. Wu, L. Guo, Z. Liu, and G. Peng, Production of proton-rich nuclei in the vicinity of ^{100}Sn via multinucleon transfer reactions, Phys. Lett. B **825**, 136886 (2022).

[18] C. Simenel, D. J. Hinde, R. du Rietz, M. Dasgupta, M. Evers, C. J. Lin, D. H. Luong, and A. Wakhle, Influence of entrance-channel magicity and isospin on quasi-fission, Phys. Lett. B **710**, 607 (2012).

[19] D. J. Hinde, M. Dasgupta, J. R. Leigh, J. C. Mein, C. R. Morton, J. O. Newton, and H. Timmers, Conclusive evidence for the influence of nuclear orientation on quasifission, Phys. Rev. C **53**, 1290 (1996).

[20] G. N. Knyazheva, E. M. Kozulin, R. N. Sagaidak, A. Yu. Chizhov, M. G. Itkis, N. A. Kondratiev, V. M. Voskressensky, A. M. Stefanini, B. R. Behera, L. Corradi, E. Fioretto, A. Gadea, A. Latina, S. Szilner, M. Trotta, S. Beghini, G. Montagnoli, F. Scarlassara, F. Haas, N. Rowley *et al.*, Quasifission processes in ^{40,48}Ca + ^{144,154}Sm reactions, Phys. Rev. C **75**, 064602 (2007).

[21] K. Nishio, H. Ikezoe, S. Mitsuoka, I. Nishinaka, Y. Nagame, Y. Watanabe, T. Ohtsuki, K. Hirose, and S. Hofmann, Effects of nuclear orientation on the mass distribution of fission fragments in the reaction of ^{36}S + ^{238}U, Phys. Rev. C **77**, 064607 (2008).

[22] T. K. Ghosh, S. Pal, T. Sinha, S. Chattopadhyay, P. Bhattacharya, D. C. Biswas, and K. S. Golda, Anomalous increase in width of fission-fragment mass distribution as a probe for onset of quasifission reactions in deformed target-projectile system at near and sub-barrier energies, Phys. Rev. C **70**, 011604(R) (2004).

[23] A. Wakhle, C. Simenel, D. J. Hinde, M. Dasgupta, M. Evers, D. H. Luong, R. du Rietz, and E. Williams, Interplay between quantum shells and orientation in quasifission, Phys. Rev. Lett. **113**, 182502 (2014).

[24] B. B. Back, P. B. Fernandez, B. G. Glagola, D. Henderson, S. Kaufman, J. G. Keller, S. J. Sanders, F. Videbæk, T. F. Wang, and B. D. Wilkins, Entrance-channel effects in quasifission reactions, Phys. Rev. C **53**, 1734 (1996).

[25] D. J. Hinde, M. Dasgupta, and A. Mukherjee, Severe inhibition of fusion by quasifission in reactions forming ^{220}Th, Phys. Rev. Lett. **89**, 282701 (2002).

[26] R. Rafiei, R. G. Thomas, D. J. Hinde, M. Dasgupta, C. R. Morton, L. R. Gasques, M. L. Brown, and M. D. Rodriguez, Strong evidence for quasifission in asymmetric reactions forming ^{202}Po, Phys. Rev. C **77**, 024606 (2008).

[27] E. M. Kozulin, G. N. Knyazheva, T. K. Ghosh, A. Sen, I. M. Itkis, M. G. Itkis, K. V. Novikov, I. N. Diatlov, I. V. Pchelintsev, C. Bhattacharya, S. Bhattacharya, K. Banerjee, E. O. Saveleva, and I. V. Vorobiev, Fission and quasifission of the composite system Z = 114 formed in heavy-ion reactions at energies near the Coulomb barrier, Phys. Rev. C **99**, 014616 (2019).

[28] I. M. Itkis, E. M. Kozulin, M. G. Itkis, G. N. Knyazheva, A. A. Bogachev, E. V. Chernysheva, L. Krupa, Yu. Ts. Oganessian, V. I. Zagrebaev, A. Ya. Rusanov, F. Goennenwein, O. Dorvaux, L. Stuttgé, F. Hanappe, E. Vardaci, and E. de Goés Brennand, Fission and quasifission modes in heavy-ion-induced reactions leading to the formation of Hs*, Phys. Rev. C **83**, 064613 (2011).

[29] E. M. Kozulin, V. I. Zagrebaev, G. N. Knyazheva, I. M. Itkis, K. V. Novikov, M. G. Itkis, S. N. Dmitriev, I. M. Harca, A. E. Bondarchenko, A. V. Karpov, V. V. Saiko, and E. Vardaci, Inverse quasifission in the reactions ^{156,160}Gd + ^{186}W, Phys. Rev. C **96**, 064621 (2017).

[30] A. S. Umar, V. E. Oberacker, and C. Simenel, Fusion and quasifission dynamics in the reactions ^{48}Ca + ^{249}Bk and ^{50}Ti + ^{249}Bk using a time-dependent Hartree-Fock approach, Phys. Rev. C **94**, 024605 (2016).

[31] K. Hammerton, Z. Kohley, D. J. Hinde, M. Dasgupta, A. Wakhle, E. Williams, V. E. Oberacker, A. S. Umar, I. P. Carter, K. J. Cook, J. Greene, D. Y. Jeung, D. H. Luong, S. D. McNeil, C. S. Palshetkar, D. C. Rafferty, C. Simenel, and K. Stiefel, Reduced quasifission competition in fusion reactions forming neutron-rich heavy elements, Phys. Rev. C **91**, 041602(R) (2015).

[32] T. Nakatsukasa, K. Matsuyanagi, M. Matsuo, and K. Yabana, Time-dependent density-functional description of nuclear dynamics, Rev. Mod. Phys. **88**, 045004 (2016).

[33] V. E. Oberacker, A. S. Umar, and C. Simenel, Dissipative dynamics in quasifission, Phys. Rev. C **90**, 054605 (2014).

[34] A. S. Umar, V. E. Oberacker, and C. Simenel, Shape evolution and collective dynamics of quasifission in the time-dependent Hartree-Fock approach, Phys. Rev. C **92**, 024621 (2015).

[35] K. Sekizawa and K. Yabana, Time-dependent Hartree-Fock calculations for multinucleon transfer and quasifission processes in the ^{64}Ni + ^{238}U reaction, Phys. Rev. C **93**, 054616 (2016).

[36] K. Sekizawa, Microscopic description of production cross sections including deexcitation effects, Phys. Rev. C **96**, 014615 (2017).

[37] C. Simenel, Particle transfer reactions with the time-dependent Hartree-Fock theory using a particle number projection technique, Phys. Rev. Lett. **105**, 192701 (2010).

[38] C. Simenel, K. Godbey, and A. S. Umar, Timescales of quantum equilibration, dissipation and fluctuation in nuclear collisions, Phys. Rev. Lett. **124**, 212504 (2020).

[39] C. Simenel, Nuclear quantum many-body dynamics, Eur. Phys. J. A **48**, 152 (2012).

[40] C. Simenel and A. S. Umar, Heavy-ion collisions and fission dynamics with the time–dependent Hartree-Fock theory and its extensions, Prog. Part. Nucl. Phys. **103**, 19 (2018).

[41] Kazuyuki Sekizawa, TDHF theory and its extensions for the multinucleon transfer reaction: A mini review, Front. Phys. **7**, 20 (2019).

[42] P. D. Stevenson and M. C. Barton, Low–energy heavy-ion reactions and the Skyrme effective interaction, Prog. Part. Nucl. Phys. **104**, 142 (2019).

[43] S. Ayik and K. Sekizawa, Kinetic-energy dissipation and fluctuations in strongly damped heavy-ion collisions within the stochastic mean-field approach, Phys. Rev. C **102**, 064619 (2020).

[44] M. Tohyama and A. S. Umar, Quadrupole resonances in unstable oxygen isotopes in time-dependent density-matrix formalism, Phys. Lett. B **549**, 72 (2002).

[45] M. Tohyama, Applications of time-dependent density-matrix approach, Front. Phys. **8**, 67 (2020).

[46] C. Simenel, Particle-number fluctuations and correlations in transfer reactions obtained using the Balian-Vénéroni variational principle, Phys. Rev. Lett. **106**, 112502 (2011).

[47] S. Ayik, A stochastic mean-field approach for nuclear dynamics, Phys. Lett. B **658**, 174 (2008).

[48] D. Lacroix and S. Ayik, Stochastic quantum dynamics beyond mean field, Eur. Phys. J. A **50**, 95 (2014).

[49] R. Balian and M. Vénéroni, Time-dependent variational principle for the expectation value of an observable: Mean-field applications, Ann. Phys. (NY) **164**, 334 (1985).

[50] R. Balian and M. Vénéroni, Correlations and fluctuations in static and dynamic mean-field approaches, Ann. Phys. (NY) **216**, 351 (1992).

[51] E. Williams, K. Sekizawa, D. J. Hinde, C. Simenel, M. Dasgupta, I. P. Carter, K. J. Cook, D. Y. Jeung, S. D. McNeil, C. S. Palshetkar, D. C. Rafferty, K. Ramachandran, and A. Wakhle, Exploring zeptosecond quantum equilibration dynamics: From deep-inelastic to fusion-fission outcomes in ^{58}Ni + ^{60}Ni reactions, Phys. Rev. Lett. **120**, 022501 (2018).

[52] K. Godbey and A. S. Umar, Quasifission dynamics in microscopic theories, Front. Phys. **8**, 40 (2020).

[53] K. Godbey, C. Simenel, and A. S. Umar, Microscopic predictions for the production of neutron-rich nuclei in the reaction ^{176}Yb + ^{176}Yb, Phys. Rev. C **101**, 034602 (2020).

[54] A. Sen, T. K. Ghosh, E. M. Kozulin, I. M. Itkis, G. N. Knyazheva, K. V. Novikov, S. Bhattacharya, K. Banerjee, and C. Bhattacharya, Quasifission in ^{84,86}Kr-induced reactions populating superheavy elements, Phys. Rev. C **105**, 014627 (2022).

[55] E. M. Kozulin, G. N. Knyazheva, I. M. Itkis, M. G. Itkis, A. A. Bogachev, E. V. Chernysheva, L. Krupa, F. Hanappe, O. Dorvaux, L. Stuttgé, W. H. Trzaska, C. Schmitt, and G. Chubarian, Fusion-fission and quasifission of superheavy systems with Z = 110–116 formed in ^{48}Ca-induced reactions, Phys. Rev. C **90**, 054608 (2014).

[56] A. S. Umar, M. R. Strayer, J. S. Wu, D. J. Dean, and M. C. Güçlü, Nuclear Hartree-Fock calculations with splines, Phys. Rev. C **44**, 2512 (1991).

[57] A. S. Umar and V. E. Oberacker, Three-dimensional unrestricted time-dependent Hartree-Fock fusion calculations using the full Skyrme interaction, Phys. Rev. C **73**, 054607 (2006).

[58] K.-H. Kim, T. Otsuka, and P. Bonche, Three-dimensional TDHF calculations for reactions of unstable nuclei, J. Phys. G: Nucl. Part. Phys. **23**, 1267 (1997).

[59] W. Q. Shen, J. Albinski, A. Gobbi, S. Gralla, K. D. Hildenbrand, N. Herrmann, J. Kuzminski, W. F. J. Müller, H. Stelzer, J. Tõke, B. B. Back, S. Bjørnholm, and S. P. Sørensen, Fission and quasifission in U-induced reactions, Phys. Rev. C **36**, 115 (1987).

[60] See Supplemental Material at http://link.aps.org/supplemental/10.1103/PhysRevC.108.064604 for an extended discussion of the calculations presented in this work.

[61] C. W. Gardiner, *Quantum Noise* (Springer-Verlag, Berlin, 1991)

[62] A. C. Merchant and W. Nörenberg, Microscopic transport theory of heavy-ion collisions, Z. Phys. A **308**, 315 (1982).

[63] K. Sekizawa and S. Ayik, Quantal diffusion approach for multinucleon transfer processes in the ^{58,64}Ni + ^{208}Pb reactions: Toward the production of unknown neutron-rich nuclei, Phys. Rev. C **102**, 014620 (2020).

[64] S. Ayik, M. Arik, O. Yilmaz, B. Yilmaz, and A. S. Umar, Multinucleon transfer mechanism in ^{250}Cf + ^{232}Th collisions using the quantal transport description based on the stochastic mean-field approach, Phys. Rev. C **107**, 014609 (2023).

[65] S. Ayik, M. Arik, E. C. Karanfil, O. Yilmaz, B. Yilmaz, and A. S. Umar, Quantal diffusion description of isotope production via the multinucleon transfer mechanism in ^{48}Ca + ^{238}U collisions, Phys. Rev. C **104**, 054614 (2021).

[66] S. Ayik, B. Yilmaz, O. Yilmaz, and A. S. Umar, Merging of transport theory with the time-dependent Hartree-Fock approach: Multinucleon transfer in U + U collisions, Phys. Rev. C **102**, 024619 (2020).

[67] S. Ayik, B. Yilmaz, O. Yilmaz, and A. S. Umar, Quantal diffusion approach for multinucleon transfers in Xe + Pb collisions, Phys. Rev. C **100**, 014609 (2019).

[68] S. Ayik, O. Yilmaz, B. Yilmaz, and A. S. Umar, Heavy-isotope production in ^{136}Xe + ^{208}Pb collisions at $E_{\mathrm{c.m.}} = 514$ MeV, Phys. Rev. C **100**, 044614 (2019).

[69] B. Yilmaz, S. Ayik, O. Yilmaz, and A. S. Umar, Multinucleon transfer in ^{58}Ni + ^{60}Ni and ^{60}Ni + ^{60}Ni in a stochastic mean-field approach, Phys. Rev. C **98**, 034604 (2018).

[70] O. Yilmaz, G. Turan, and B. Yilmaz, Quasi-fission and fusion-fission reactions in ^{48}Ca + ^{208}Pb collisions at $E_{\mathrm{c.m.}} = 190$ MeV, Eur. Phys. J. A **56**, 37 (2020).

[71] S. Ayik, B. Yilmaz, O. Yilmaz, A. S. Umar, and G. Turan, Multinucleon transfer in central collisions of ^{238}U + ^{238}U, Phys. Rev. C **96**, 024611 (2017).

[72] S. Ayik, B. Yilmaz, O. Yilmaz, and A. S. Umar, Quantal diffusion description of multinucleon transfers in heavy–ion collisions, Phys. Rev. C **97**, 054618 (2018).

[73] W. U. Schröder, J. R. Huizenga, and J. Randrup, Correlated mass and charge transport induced by statistical nucleon exchange in damped nuclear reactions, Phys. Lett. B **98**, 355 (1981).

[74] U. Weiss, *Quantum Dissipative Systems*, 2nd ed. (World Scientific, Singapore, 1999).

[75] H. Risken and T. Frank, *The Fokker–Planck Equation* (Springer-Verlag, Berlin, 1996).

[76] R. Charity, GEMINI: A code to simulate the decay of a compound nucleus by a series of binary decays, Technical Report (2008).